Diffusive motion of a semirigid fiber immersed in a granular flow

Kennedy Nexon Chagua Encarnación, Antoine Seguin, Baptiste Darbois Texier

Diffusive motion of a semirigid fiber immersed in a granular flow

Kennedy Nexon Chagua Encarnación,[1] Antoine Seguin,[1] and Baptiste Darbois Texier[1,*]

[1]*Université Paris-Saclay, CNRS, Laboratoire FAST, 91405 Orsay, France*

(Dated: February 11, 2026)

This study investigates the diffusive motion of a semirigid fiber immersed in a dense granular packing. Experiments are conducted in an index-matched medium composed of water-saturated hydrogel beads, which is sheared by means of a rotating paddle. In the quasistatic regime, we first characterize the self-diffusion of individual grains and show that it follows established scaling laws for granular diffusion. We then analyze the motion of a single fiber for various imposed shear rates and for different fiber and grain dimensions. We show that the fiber undergoes a slow and steady settling through the medium, with a sedimentation velocity that decreases as the fiber length increases relative to the grain size. After removing this mean settling motion, we find that the residual vertical displacement of the fiber exhibits a diffusive behavior. The effective diffusion coefficient decreases with increasing fiber length and is primarily governed by the ratio of fiber length to grain diameter. From these results, we derive an empirical relationship for the fiber diffusion coefficient in granular flow, expressed as a function of both fiber and flow properties.

I. INTRODUCTION

In dense granular flows, collisions between grains induce velocity fluctuations that lead to particle diffusion, resembling thermal diffusion of Brownian particles. Understanding and quantifying this diffusive behavior of grains is crucial for accurately describing mixing and segregation phenomena [1], which are of first importance in numerous industrial processes involving granular materials. Granular diffusion has been investigated using a combination of experimental and numerical methods across various flow configurations, including simple shear flows [2, 3], inclined planes, Couette cells [4] and rotating drums. These studies have demonstrated that the long-term dynamics of a particle in dense granular flows can be characterized by an effective diffusion coefficient, K. This coefficient K depends on the grain diameter d_g and the flow shear rate $\dot{\gamma}$ through the Bagnold scaling which expresses:

$$K = f(\phi)\, d_g^2 \dot{\gamma} \tag{1}$$

where f is a function that depends solely on the packing fraction ϕ of the granular medium [5]. Depending on the flow configurations and flow regimes, different expressions of f have been determined. In a two-dimensional (2D) Couette geometry with a large gap, Utter and Behringer [4] observed experimentally that the radial diffusion of grains follows the relationship $K \simeq 0.1\, {d_g}^2 \dot{\gamma}$, indicating a constant prefactor $f(\phi) \simeq 0.1$. Numerical simulations of grains in a simple shear flow have shown that the diffusion coefficient in the direction transverse to the flow satisfies the relation $K \simeq 0.04\, {d_g}^2 \dot{\gamma}$ [2, 3]. The variability observed in the prefactor can be attributed to a dependence of the function f on the volume fraction ϕ. In discrete element method (DEM) simulations of size-bidisperse spheres subjected to simple shear flow, Cai *et al.* [6] demonstrated that diffusion coefficients measured at different packing fractions conform to Bagnold scaling, with the prefactor described by the relation $f(\phi) = 0.0186/\phi$. Based on numerical simulations in simple shear flow where the pressure is imposed, Athani *et al.* [7] proposed an alternative expression for the function f to rationalize the diffusion coefficient K, given by $f(\phi) = 0.027\,(\phi_c - \phi)^{-1/2}$, where ϕ_c is the critical packing fraction corresponding to the jamming transition. Equivalently, this relation can be reformulated in terms of the inertial number of the granular flow, I, defined as $I = d_g\dot{\gamma}/\sqrt{P/\rho_g}$, where P is the pressure applied to the grains and ρ_g their density. Since ϕ is a unique function of I, the function f can be rewritten as $f(I) = 0.049/\sqrt{I}$. This relation was shown to accurately describe their simulation results over more than two orders of magnitude in shear rate. In addition, their study examined the influence of an interstitial viscous fluid on particle diffusion and proposed a unified framework to describe both particle diffusion in dry granular flows and particle migration in dense suspensions. Fan *et al.* [8] reported a non-Bagnoldian diffusion regime at very low shear rates, where the diffusion coefficient is independent of shear rate and arises from elastic rearrangements in the material. Some studies on particle diffusion in granular flows have also focused on the anisotropic nature of the diffusion coefficient [9, 10], i.e. the fact that K varies depending on the direction considered. In a 2D Couette configuration, it has been shown that the diffusion coefficient along the tangential direction is about twice that along the radial direction [4]. To account for diffusion anisotropy, Artoni *et al.* [3] introduced a self-diffusion tensor and analyzed its components individually. They showed that the diffusion coefficient along the flow direction is larger than in other directions.

* Contact author: baptiste.darbois-texier@universite-paris-saclay.fr

These results demonstrate that significant progress has been made in understanding the diffusion behavior of spherical particles. The case of a granular medium composed of non spherical particles has been explored by Kumar *et al.* in a rotating drum [11, 12]. They observed that segregation depends on the packing fraction and the angularity of the particle, with elongated particles being more prone to mixing. Numerical studies of the self-diffusion of spherocylindrical particles on an inclined plane have shown that Bagnold scaling described in Eq. (1) remains valid when diffusion is expressed in terms of an effective particle size. This effective size is defined as the diameter of a circle whose area matches that of the particle's orthographic projection [13]. However, much less is known about the diffusion of non-spherical particles—such as fibers—in dense granular flows composed of spherical grains. While the behavior of a single fiber in a viscous fluid has been investigated experimentally [14–16], numerically [17–19], and theoretically [20], the dynamics of a fiber in a granular flow remain largely unexplored. The presence of multiple characteristic length scales for non-spherical particles raises the fundamental question of which scale governs diffusion, presenting a major challenge for extending current diffusion models. Moreover, fiber dynamics in granular flows play a key role in applications aimed at reinforcing granular materials through fiber addition, such as in fiber-reinforced soils or concretes [21, 22]. A better understanding of how the mixing process influences the distribution of fibers within the grains should help improve the performance of fiber-reinforcement techniques.

To address this gap, we investigate the dynamics of a single fiber in a dense granular flow composed of spherical particles. The granular medium consists of saturated hydrogel beads immersed in water to achieve optical index matching, enabling the tracking of a dark fiber. The flow is generated by a paddle rotating about a vertical axis, which induces a diffusive motion of the hydrogel beads. We measure the three-dimensional dynamics of the fiber under varying conditions, including flow shear rate, bead size, fiber length and diameter. The analysis of the fiber trajectories in terms of mean-square displacement (MSD) provides an estimate of the effective diffusion coefficient along the vertical direction, transverse to the flow. We investigate how this diffusion coefficient depends on key parameters of the system and seek an empirical relationship that captures the fiber's diffusive dynamics as a function of these parameters.

The paper is organized as follows. In Sec. II, we describe the experimental setup. Sec. III presents the characterization of the stationary granular flow (Sec. III A) and self-diffusion of grains (Sec. III B). In Sec. III C, we focus on the behavior of single fibers immersed within the granular flow, examining both their sedimentation velocity (Sec. III C 1) and diffusive dynamics (Sec. III C 2). Finally, conclusions and perspectives are discussed in Sec. IV.

II. EXPERIMENTAL SETUP

The setup is sketched in Fig. 1(a) and consists of a glass rectangular reservoir of width $2w = 17$ cm and height 22 cm. The reservoir is filled with water-saturated hydrogel beads (sodium polyacrylate [1]) and distilled water (density ρ_w=1.0 $\times 10^3$ kg m^{-3}) mixed at a mass ratio of 1.88 between hydrogel beads and fluid for a total filling height $2H = 16.5$ cm. Two sizes of hydrogel beads are used: small beads with a diameter of $d_g = 10.0 \pm 0.5$ mm and a density $\rho_g = 1.03 \pm 0.02 \times 10^3$ kg m^{-3}, and large beads with a diameter of $d_g = 16.0 \pm 0.4$ mm and a density $\rho_g = 1.04 \pm 0.02 \times 10^3$ kg m^{-3}. The water-saturated hydrogel beads have a refractive index close to that of the interstitial water, providing index-matching conditions that enable visualization throughout the bulk of the granular medium [24]. A few hydrogel beads were also colored to distinguish them from the transparent ones, enabling their position to be tracked within the reservoir. The granular medium is set in motion by a comb-shaped paddle [see Fig. 1(b)] positioned at the center of the reservoir and driven by a *DC* gear motor (RoHS 921-1451), which maintains a constant rotational speed around the vertical axis z. The paddle is made of poly(methyl methacrylate) with a refractive index of 1.49, slightly higher than that of water (1.33), making it sufficiently transparent to avoid perturbing the visualization of grains and fibers during the experiment. The paddle has a total size of 160×200 mm and has four rectangular branches of 10 mm width, each separated by a distance of 40 mm [see Fig. 1(b)]. The geometry and dimensions of the paddle are selected to ensure the transmission of the rotation to the grains while limiting grains clogging between the branches of the paddle [25]. The rotation speed of the paddle ω is controlled by adjusting the supply voltage of the DC gear motor and can be varied between 0.2 and 2.0 rad.s^{-1}. In this configuration, the gravitational field, g, acts in the direction perpendicular to the plane of rotation of the grains. In addition to hydrogel beads, a single fiber with a length of l_f and a diameter of d_f can also be placed at the center of the reservoir. We use fibers made of nitrile rubber with a density of 1.3×10^3 kg m^{-3} with diameters ranging from $1 < d_f < 3.5$ mm and lengths ranging from $5 < l_f < 30$ mm. Nitrile rubber, with a Young's modulus of $E \simeq 7$ MPa, makes the fibers flexible; modeled as elastic beams subjected to a pressure difference between their two ends, their typical normalized deflection ξ/l_f is estimated between 2×10^{-6} and 1×10^{-1}, indicating small deformations and classifying them as semirigid fibers. This pressure arises from the slight density difference between the hydrogel beads and the surrounding fluid, resulting in a depth-dependent granular pressure. The fibers are black, making them detectable within the reservoir filled with hydrogel beads and water. To track the dynamic of colored hydrogel beads or dark fibers placed in the granular flow generated by the rotation of the paddle, we use two

[1] For more information, see Ref. [23]

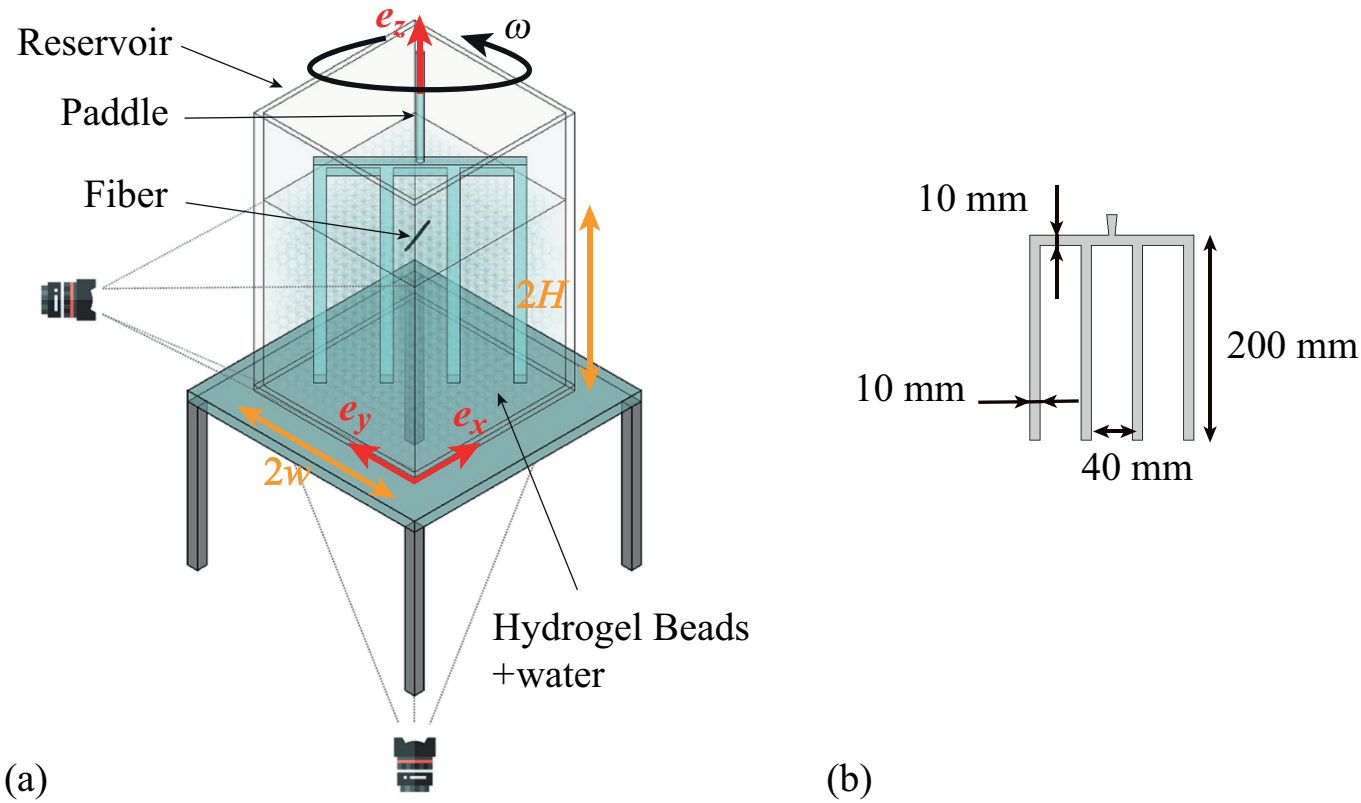

FIG. 1: (a) Sketch of the experimental setup used to study the dynamics of a single fiber in a dense granular flow. (b) Dimensions of the paddle used to impose the granular flow.

cameras (NIKON D3500) placed at the side and the bottom of the reservoir, respectively. The videos are acquired at a frame rate of 2 Hz for a duration of 5 min or until the fiber reaches the edge of the container or the upper surface of the granular medium. The resolution of the images obtained with these cameras is about 0.15 mm/pixel. The videos are then analyzed with the FIJI software [26] by conversion to grayscale and segmentation. From the segmented images, we perform single particle tracking using the Python programming language and the trackpy Python library [27]. We also apply depth correction on the detection of the position of the colored hydrogel beads and fiber to account for the distance of the object with the cameras. This procedure allows us to reconstruct the three-dimensional (3D) trajectory of the center of mass of the particle whether a colored hydrogel bead or a fiber. Figures 2(a) and 2(b) present the reconstructed trajectory of two black hydrogel beads entrained by the rotation of the paddle as viewed from the bottom and the side. The reconstructed trajectories of a short and a long fiber entrained by the granular flow are presented in Figs. 2(c), 2(d) and 2(e), 2(f), respectively. The position of the center of mass of the object (colored hydrogel bead or fiber) at a given time is denoted as point P and its coordinates can be expressed in the Cartesian reference frame $(\mathbf{e}_x, \mathbf{e}_y, \mathbf{e}_z)$ as $\mathbf{OP} = x(t)\mathbf{e}_x + y(t)\mathbf{e}_y + z(t)\mathbf{e}_z$ or in the cylindrical reference frame $(\mathbf{e}_r, \mathbf{e}_\theta, \mathbf{e}_z)$ as $\mathbf{OP} = r(t)\mathbf{e}_r + z(t)\mathbf{e}_z$, where $\mathbf{e}_r = \cos\theta\,\mathbf{e}_x + \sin\theta\,\mathbf{e}_y$. The origin O of these two reference frames is defined by the intersection between the vertical axis of the reservoir and its bottom plane (Fig 2). To assess data dispersion, ten experiments were performed for each experimental condition, yielding one trajectory per condition. Grain trajectories contain approximately 700 points. Fiber trajectories vary in length depending on the experimental conditions: short fibers produce around 80 points, whereas long fibers can reach up to 700 points.

Since water is used as the interstitial fluid between the beads, it is relevant to determine the granular flow regime under which the experiments are conducted. This can be achieved by calculating the Stokes number, St, which represents the ratio of the inertial stress $\rho_g\, {d_g}^2 \dot{\gamma}^2$ to the viscous stress $\eta\dot{\gamma}$ [28, 29], where η is the fluid's dynamic viscosity ($\eta = 1.0$ mPa.s for water at 20°C), and is given by $\mathrm{St} = \rho_g {d_g}^2 \dot{\gamma}/\eta$. To estimate St for our system, we assume that the flow shear rate, $\dot{\gamma}$, scales with the paddle's rotation speed, ω, providing a reasonable approximation of its typical value. Under the described experimental conditions, St ranges from 30 to 350, well above unity. This indicates that viscous stresses are negligible compared to inertial stresses, allowing the viscous effects of the surrounding fluid to be disregarded. Consequently, the presence of water as an interstitial fluid serves solely for index-matching and visualization purposes.

Since hydrogel beads do not have neutral buoyancy and their density is slightly higher than that of water, a confinement pressure P is established in the medium. This pressure is described by a hydrostatic-like pressure profile $P = \Delta\rho g h$ where $\Delta\rho = \rho_g - \rho_w$

is the difference in density between the grain and water, and depth h is the vertical distance from the free surface ($0 \leq h \leq 2H$). For a particle located in the flow whose vertical position fluctuates around its mean position z_m (corresponding to a mean depth $h_m = 2H - z_m$), we can define the associated inertial number $I = \dot{\gamma} d_g / \sqrt{\Delta \rho g h_m / \rho_g}$. Under our experimental conditions, we can estimate that the inertial number I varies between 3×10^{-3} and 10^{-1}, corresponding to the quasistatic regime of granular flows [30]. Furthermore, vertical fluctuations in particle positions generate variations in their associated number I that are sufficiently small to consider this number I as constant during its displacement.

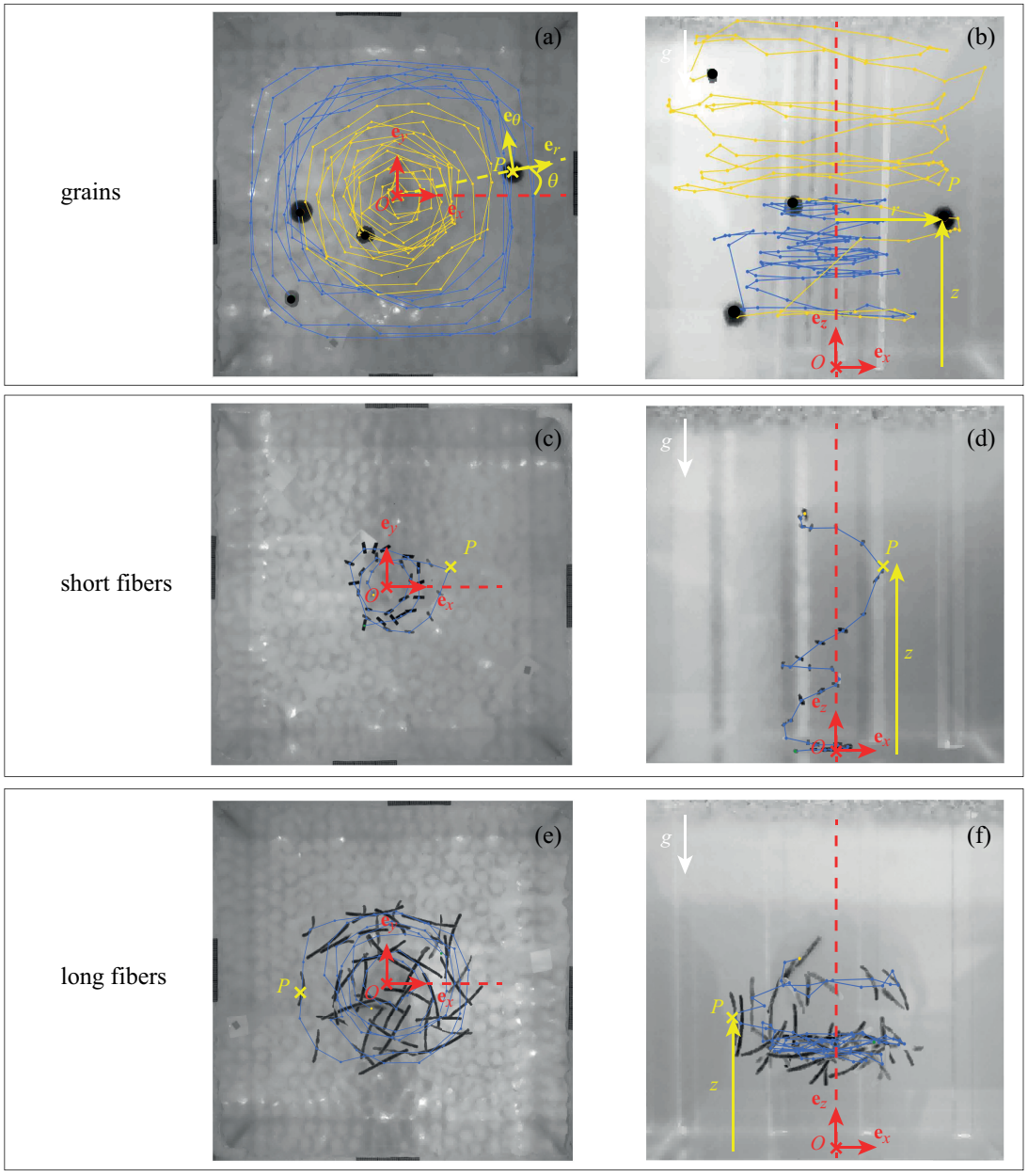

FIG. 2: Bottom and front views of the experiment with reconstructed trajectories of different particles: (a), (b) colored hydrogel beads, (c), (d) a short fiber and (e), (f) a long fiber. Panels (a), (c), (e) correspond to bottom views and (b), (d), (f) to front views. (a), (b) Hydrogel beads colored in black with a diameter d_g =10 mm. (c), (d) Short fibers of length l_f = 5 mm and diameter d_f = 1.6 mm diameter. (e), (f) Long fibers of length l_f = 30 mm and diameter d_f = 1.6 mm. The blue and yellow solid lines with markers represent the trajectories of the tracked objects in each image. The current location of the tracked object is indicated by the point P , shown in both the Cartesian reference frame $(\mathbf{e}_x, \mathbf{e}_y, \mathbf{e}_z)$ and the cylindrical reference frame $(\mathbf{e}_r, \mathbf{e}_\theta, \mathbf{e}_z)$, with O as the common origin of both frames.

III. RESULTS

In this section, we first present the experimental results of the mean granular flow induced by the rotation of the paddle. Then, we focus on the analysis of fiber dynamics within the granular flow as a function of the flow's characteristics and the fiber properties.

A. Stationary granular flow

To characterize the steady-state granular flow induced by the motion of the paddle, we analyze the trajectories of few dark hydrogel beads dispersed among transparent beads of identical size. Figure 3(a) shows ten trajectories of hydrogel beads (d_g =10 mm) in identical flow conditions (ω = 2.0 rad.s^{-1}), each starting from a different initial position within the reservoir. We observe that beads follow the global rotation induced by the paddle while exploring different radial and vertical positions during their trajectories. Figures 3(b)-3(d) present the angular, radial and vertical coordinates of the beads along their trajectories as a function of time. We observe that the angle θ increases continuously over time, while the radial and vertical coordinates, r and z, experience significant fluctuations, characteristic of particle diffusion in granular flows.

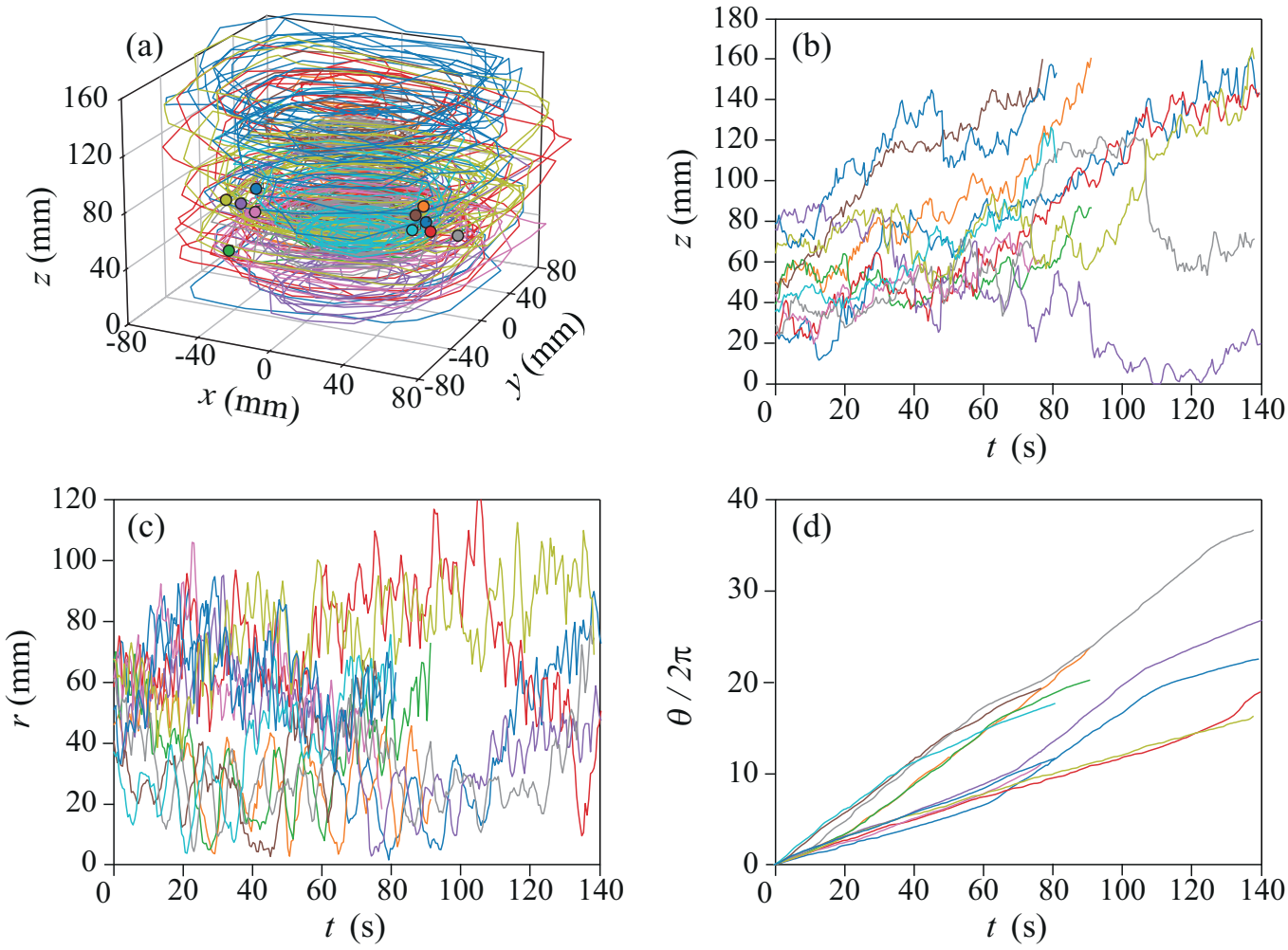

FIG. 3: (a) Ten trajectories of hydrogel beads (d_g = 10 mm) immersed in a granular flow generated by the rotation of the paddle at a rotation speed of ω = 2.0 rad.s^{-1}. Dots represent the initial positions of the grains. (b)-(d) Cylindrical coordinates of the beads along these ten different trajectories as a function of time: (b) vertical positions z, (c) radial positions r and (d) angular positions θ.

From the time evolution of the beads angular positions, we compute the average orthoradial velocity using the relation $v_\theta = \langle r \rangle \langle \dot{\theta} \rangle$, where the spatial average $\langle\,\rangle$ is taken over trajectory segments in which the radial position remains approximately

constant. Figure 4(a) presents the average orthoradial velocity of the beads v_θ as a function of their radial position r for a constant rotation speed of the paddle $\omega = 2.0$ rad.s^{-1}. Two distinct flow regions can be identified based on the distance from the center. A first region, $0 < r < r_1$, is characterized by a linear increase of v_θ with r, which can be described by the relation $v_\theta = \Omega r$, where Ω represents the average angular velocity of the grains in this region. A second region, $r_1 < r < w$, is characterized by an approximately constant orthoradial velocity v_θ. The saturation of the speed in this region can be attributed to the lateral confinement imposed by the vertical walls, which limits the flow in a central zone to a radius of approximately $r \simeq w$. Note that we exclude the motion of the beads located at the four corners of the reservoir (i.e. $r > w$) from the analysis, as their motion is not directly influenced by the rotation of the paddle. The boundary position between the two flow regions is observed to be independent of both the paddle's rotation speed and the grain diameter, with $r_1 \simeq 30$ mm. We have repeated the analysis of the average granular flow for different rotation speeds of the paddle ω and different grain diameters d_g, estimating in each case the average angular velocity Ω of the granular medium at the center of the reservoir. Figure 4(b) presents the ratio of rotation speeds, Ω/ω, as a function of the rotation speed imposed by the paddle ω for two different grain diameters. We observe that the rotation speed ratio remains constant and does not depend on either ω or d_g. We therefore conclude that the average angular velocity of the granular flow is approximately 93 % of the rotation speed of the paddle $\Omega \simeq 0.93\ \omega$.

To describe the diffusive motion driven by this global granular flow, we must consider the local flow of grains in the vicinity of each branch of the paddle. Each branch can be regarded as an intruder moving through the granular medium and generating a non-uniform flow that repeatedly shears the material. The granular flow induced by the movement of an intruder in the quasistatic regime has been studied by Seguin *et al.* [31]. They showed that an intruder moving at a velocity V within a granular medium generates a local flow surrounding the intruder, characterized by a local shear rate that scales as V/λ, where λ is the localization length of the flow and scales linearly with the size of the intruder and does not depend on its speed V. Applying this framework to our experimental setup, each paddle branch acts as an intruder moving at a velocity $V = r\omega$. The resulting local shear rate is therefore $r\omega/\lambda$. During one full rotation, each grain is influenced twice by the passage of the paddle branches. The fraction of the rotation during which a given grain is sheared is $2\lambda/2\pi r$. Hence, the average shear rate experienced by the grains corresponds to the local shear rate weighted by this fraction and expresses as $\dot{\gamma} = (r\omega/\lambda)(2\lambda/2\pi r) = \omega/\pi$. This expression will be used in the remainder of the article.

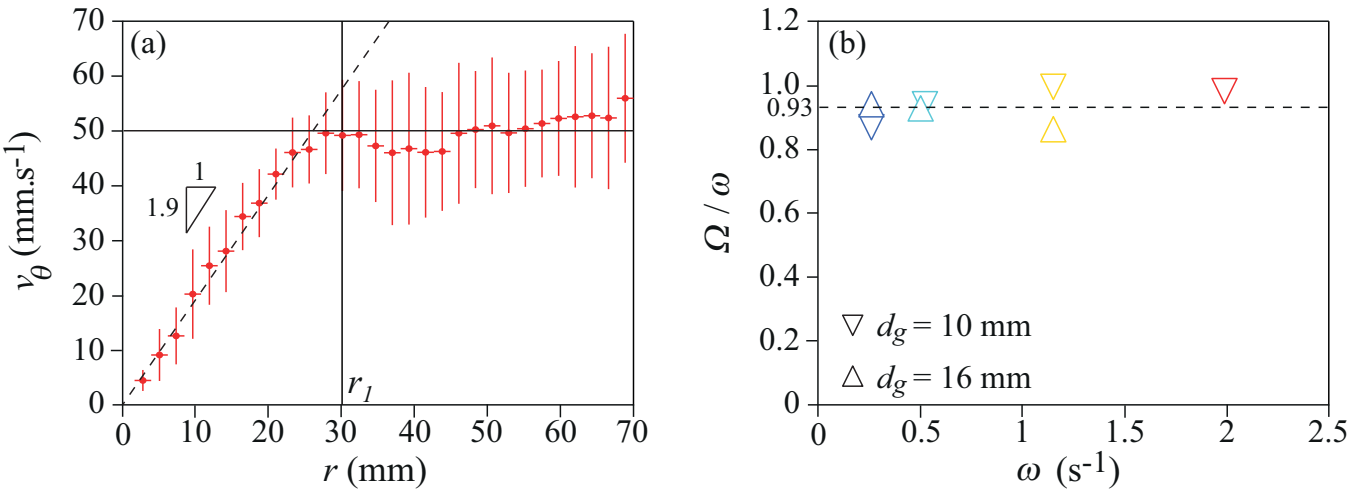

FIG. 4: (a) Orthoradial velocity of the grains v_θ as a function of their radial position r for $\omega = 2.0$ rad.s^{-1} and d_g =10 mm. The black dashed line is the best fit of the data for $r < 30$ mm, i.e. $v_\theta = \Omega r$, which provides an estimate of the average angular velocity Ω of the grains. The horizontal solid line corresponds to the saturation of the orthoradial velocity to $v_\theta \simeq 50$ mm.s^{-1}. The vertical solid line corresponds to the limit of the two flowing regions at $r_1 \simeq 30$ mm. (b) Mean angular velocity of granular flow in the central region, Ω, normalized by the imposed rotation speed of the paddle, ω, as a function of ω for two different grain diameters. The horizontal dashed line represents the mean of the data given by $\Omega/\omega \simeq 0.93$.

B. Grains diffusion coefficient

Fluctuations in grain trajectories along directions transverse to the mean flow—namely, the vertical (z) direction and the radial (r) direction shown in Fig. 3(c) and 3(d)—can, in principle, be analyzed in terms of diffusive behavior. Here, we focus exclusively on the vertical (z) direction, as the granular flow induced by the paddle couples particle dynamics in the radial (r) direction and also in the orthoradial (θ) direction, complicating the interpretation of diffusion along these directions. The relative displacement

δ_i of a grain indexed by i along the z-axis between times t and $t + \tau$ is defined as:

$$\delta_i(t, \tau) = z_i(t + \tau) - z_i(t). \tag{2}$$

The MSD of the grains, Δ_g, for a given time lag τ, is calculated by averaging the square of δ_i over the duration of the experiment and across N grain trajectories:

$$\Delta_g(\tau) = \frac{1}{N} \sum_{i=1}^{N} \frac{1}{T - \tau} \int_0^{T-\tau} \delta_i^2(t, \tau)\, dt. \tag{3}$$

Equation (3) is used to compute the MSD from the grain trajectories, such as those shown in Fig. 3. Figures 5(a) and 5(b) present Δ_g as a function of lag time τ for various rotation speeds of the paddle ω, and two different grain diameters, d_g. The data points align with a slope of one in the log-log plots, indicating a linear relationship between Δ_g and τ, characteristic of diffusive behavior. The prefactor in this relation corresponds to the diffusion coefficient of the grains, K_g, satisfying:

$$\Delta_g = 2K_g\, \tau \tag{4}$$

As shown in Fig. 5(a) and 5(b), the curves shift upward with increasing rotation speed of the granular flow or grain diameter. This observation indicates that the diffusion coefficient K_g increases with both ω and d_g. These observations are consistent with the literature, where the self-diffusion coefficient of a grain in a granular flow with shear rate $\dot{\gamma}$ has been shown to scale as $K_g \sim \dot{\gamma}\, {d_g}^2/\sqrt{I}$ [7, 32]. To assess the consistency of our measurements with this relationship, we plot in Fig. 5(c) the diffusion coefficients extracted from the fits in Figs. 5(a) and 5(b) as a function of the ratio $\dot{\gamma}\, {d_g}^2/\sqrt{I}$. In this expression, the shear rate is estimated from the paddle rotation as $\dot{\gamma} = \omega/\pi$. The data align reasonably well with a linear trend:

$$K_g = A\, \frac{\dot{\gamma} d_g^2}{\sqrt{I}}. \tag{5}$$

From the linear fit of the data, we determine the prefactor to be $A = 0.03 \pm 0.005$. Previous numerical studies have estimated the self-diffusion coefficient in dense granular flows, reporting prefactors in the range $A = 0.04$–0.05 across a wide range of solid volume fractions [3, 7, 33]. The prefactor estimated in this study is of the same order of magnitude as those reported in the literature, albeit slightly smaller—possibly due to the low friction coefficient between the hydrogel beads.

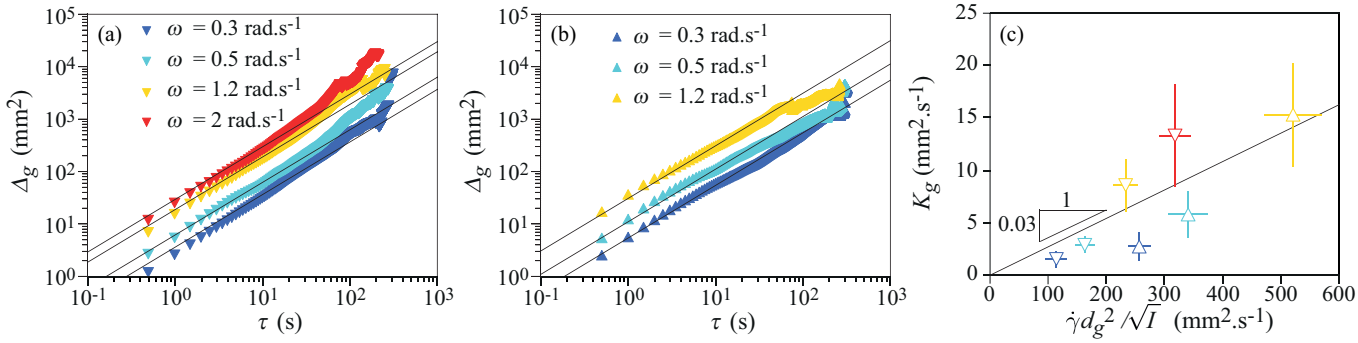

FIG. 5: (a), (b) MSD of a grain, Δ_g, as a function of lag time, τ, for different rotation speeds ω and two grain diameters: (a) d_g =10 mm (▼) and (b) d_g=16 mm (▲). The color scale corresponds to that used in Fig. 4(b) to represent rotation speed. Black lines correspond to the best fit of the data according to Eq. (4). (c) Grain diffusion coefficient K_g as a function of $\dot{\gamma} {d_g}^2/\sqrt{I}$. The solid line corresponds to the best linear fit of the data, given by $K_g = 0.03\, \dot{\gamma} {d_g}^2/\sqrt{I}$.

C. Fiber dynamics

We then focus on the dynamics of a single fiber immersed in the granular flow driven by the rotating paddle. Figure 6(a) shows the 3D trajectories of the fiber's center of mass for ten different trials conducted under identical flow conditions. The fiber has a diameter of $d_f = 1.6$ mm and a length of $l_f = 15$ mm, while the rotation speed of the paddle is set to $\omega = 1.2$ rad.s^{-1}. In

Fig. 6(a), the fiber trajectories exhibit a spiraling downward motion, in contrast to the grains in the same configuration, which undergo large vertical fluctuations accompanied by a slow upward drift over long timescales [see Fig. 3(b)]. The slow settling motion of the fiber is driven by the imposed granular flow combined with the slight density difference between the fibers and the hydrogel beads. In the following, we analyze the settling dynamics of the fiber as a function of both its intrinsic geometric properties and the characteristics of the granular flow.

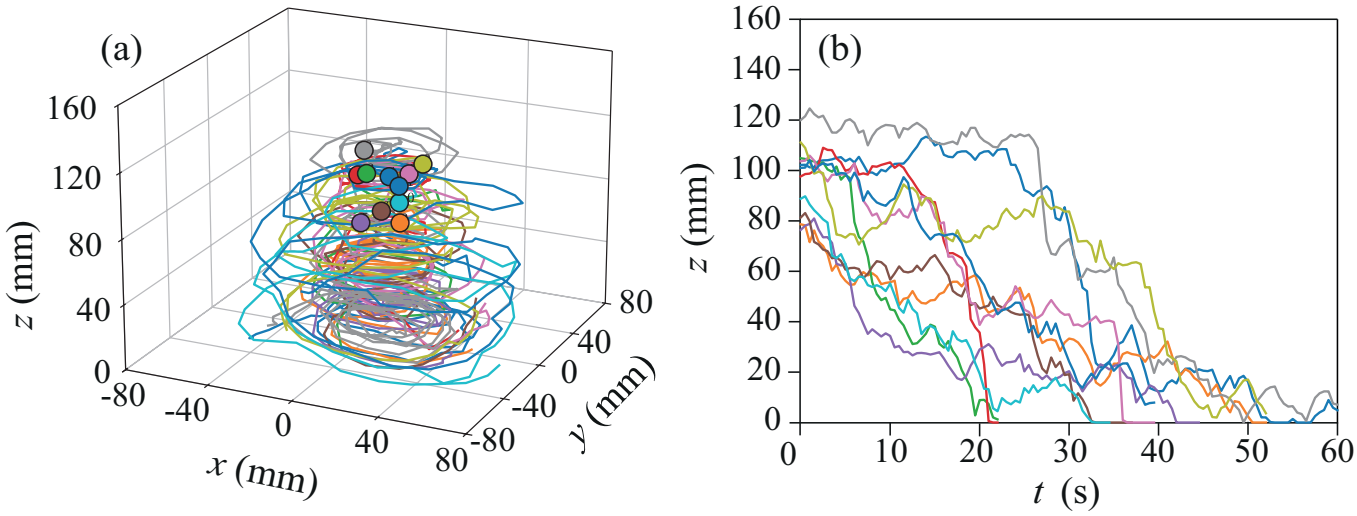

FIG. 6: (a) Three-dimensional trajectories of the center of mass of fibers of diameter $d_f = 1.6$ mm and length $l_f = 15$ mm, in grains of diameter d_g =10 mm diameter. The rotation speed of the paddle is $\omega = 1.2\,\mathrm{rad.s^{-1}}$. The round markers represent the initial positions of the fibers. (b) Vertical displacements on the z axis of these fibers extracted from panel (a) as a function of time.

1. *Sedimentation velocity*

Figure 6(b) presents the vertical position of the fiber's center of mass, z, as a function of time for the trajectories shown in Fig. 6(a). Despite the large fluctuations observed, an average sedimentation velocity, v_s, can be estimated. We measure the average vertical settling velocity of a fiber, v_s, within the granular flow for varying fiber lengths l_f, fiber diameters d_f, grain diameters d_g, and angular velocities ω of the paddle. Figure 7(a) shows v_s as a function of the ratio l_f/d_g for different angular velocities ω and fiber diameters d_f. We observe that v_s decreases rapidly with l_f/d_g, indicating that longer fibers settle at negligibly small velocities. However, no clear trends emerge regarding the influence of ω or d_f on v_s. To evaluate the role of fiber orientation on settling speed, we conducted complementary visualizations. The results reveal that fibers remain predominantly oriented within the horizontal plane, independent of their length, suggesting that orientation does not significantly affect the settling speeds measured in this study. Previous studies on the percolation of fine particles within a granular flow of larger particles have shown that small particles follow ballistic trajectories among the larger grains, with a characteristic settling velocity scaling as $v_s \sim \sqrt{g\,d_g}$ [34–36]. To examine the analogy between fine particles in larger grains and the sedimentation of short fibers in granular flow, we plot in Figure 7(b) the sedimentation velocity of a fiber, normalized by $\sqrt{gd_g}$, as a function of l_f/d_g. The inset of Fig. 7(b) presents the same data in a lin-log representation, where a reasonable collapse is observed within the experimental error bars. This suggests an empirical relationship of the form: $v_s/\sqrt{gd_g} \sim \mathrm{e}^{-\alpha\, l_f/d_g}$, with the best fit to the data obtained for $\alpha = 1.0 \pm 0.1$. We conclude that the vertical dynamics of a single fiber within a granular flow can be interpreted as a percolation-like phenomenon, and that fibers whose lengths are much greater than the grain diameter exhibit negligible sedimentation velocities.

2. *Fiber diffusion coefficient*

We now examine the diffusive dynamics of a single fiber in the granular flow. To isolate the fiber's diffusive motion along the vertical axis, we analyze its vertical position after removing the contribution from the mean sedimentation velocity. To achieve

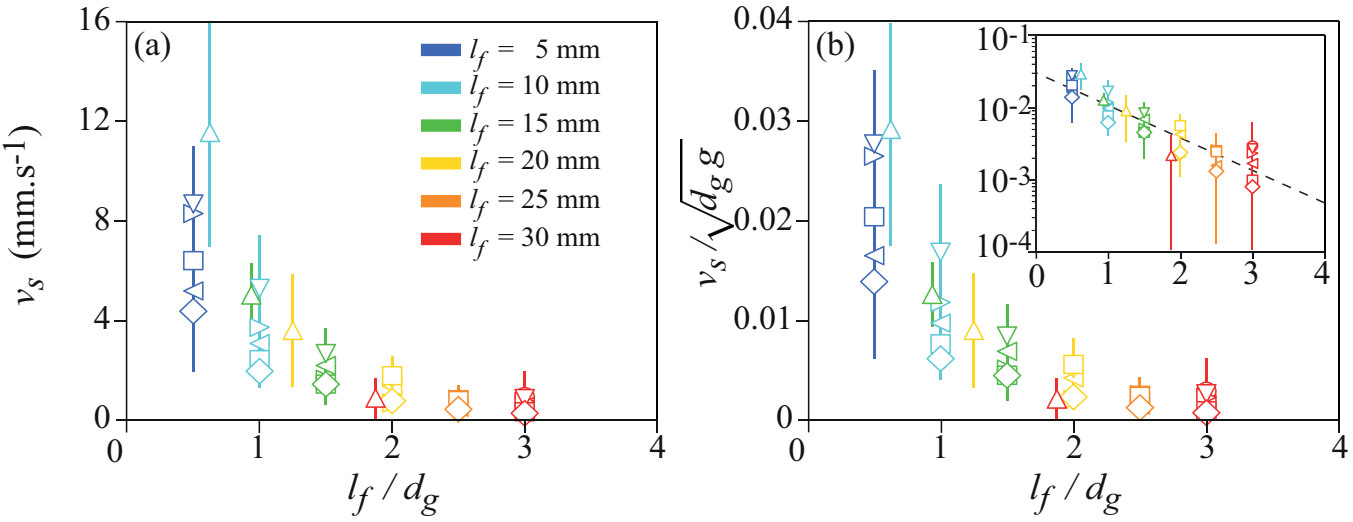

FIG. 7: (a) Mean fiber sedimentation velocity v_s as a function of l_f/d_g. Different symbols represent distinct experimental conditions: (△) d_f = 1.6 mm, d_g =16 mm, ω = 0.5 rad.s^{-1}, (▽) d_f = 1.6 mm, d_g =10 mm, ω = 0.5 rad.s^{-1}, (◁) d_f = 1.6 mm, d_g =10 mm, ω = 0.3 rad.s^{-1}, (▷) d_f = 1.6 mm, d_g =10 mm, ω = 1.2 rad.s^{-1}, (□) d_f = 2.5 mm, d_g =10 mm, ω = 1.2 rad.s^{-1}, (◇) d_f = 3.5 mm, d_g =10 mm, ω = 1.2 rad.s^{-1}. Symbol colors indicate the fiber length, l_f. (b) Fiber sedimentation velocity normalized with the characteristic velocity $\sqrt{d_g g}$ as a function of l_f/d_g. Inset: Same data in a semilog plot. The dashed line represents the best fit of the data using the expression $v_s/\sqrt{d_g g} \sim \mathrm{e}^{-\alpha\, l_f/d_g}$ where $\alpha = 1.0 \pm 0.1$.

this, we define the fiber's non-affine displacement, δ_f, over a lag time τ as

$$\delta_f(t,\tau) = z(t+\tau) + v_s\tau - z(t). \tag{6}$$

where z is the vertical position of center of mass of the fiber at a time t and v_s its average settling velocity. Then, the averaged MSD of the fiber can be computed from δ_f by averaging over time and across N independent fiber trajectories, using the relation

$$\Delta_f(\tau) = \frac{1}{N}\sum_{f=1}^{N}\frac{1}{T-\tau}\int_0^{T-\tau}\delta_f^2(t,\tau)\,dt. \tag{7}$$

We measure the dynamics of fibers of varying lengths and use Eq. (7) to compute the MSD, Δ_f, for each case. Figure 8 presents Δ_f as a function of the time lag, τ, for different l_f. In these experiments, all the other parameters were kept constants: d_f = 1.6 mm, d_g =10 mm and ω = 0.5 rad.s^{-1}. Figure 8 shows that the MSD of the fibers increase linearly with the time lag τ at short times, indicating a diffusive regime. In this regime, the MSD curves shift downward with increasing fiber length, suggesting that longer fibers exhibit slower diffusion. The data in the diffusive regime can be fitted with a linear relation of the form:

$$\Delta_f(\tau) = 2K_f\,\tau. \tag{8}$$

Here, K_f denotes the diffusion coefficient of the fiber within the granular flow. The best fits to the data using Eq. (8) are shown as dark solid lines in Fig.8. Note that the drops in the MSD observed at large time lags τ are excluded from the fitting procedure, as they result from the use of corrected trajectories in which the mean settling velocity has been subtracted. The diffusion coefficients obtained from this fitting procedure, normalized by $\dot{\gamma}{d_g}^2/\sqrt{I}$, are presented in Fig. 9(a) as a function of fiber length l_f. The results indicate that the normalized diffusion coefficient decreases with increasing fiber length, approximately following a power-law scaling of l_f^{-1}. Using the same protocol, we estimate the diffusion coefficients of fibers with identical lengths but varying diameters. Figure 9(b) shows the normalized diffusion coefficient of a fiber as a function of fiber diameter d_f for two different fiber lengths. Despite some data scatter, no clear dependence on fiber diameter is observed. We then study the influence of grain diameter on the fiber diffusion coefficient. Figure 9(c) shows the normalized diffusion coefficient of a fiber as a function of grain diameter d_g for three different fiber lengths. Although experiments are conducted with only two distinct grain diameters, the results indicate that the normalized diffusion coefficient increases with d_g. The separate observations of parameter dependencies are compiled in Fig. 10(a), which shows the normalized diffusion coefficient $K_f\sqrt{I}/(\dot{\gamma}{d_g}^2)$ as a function of the

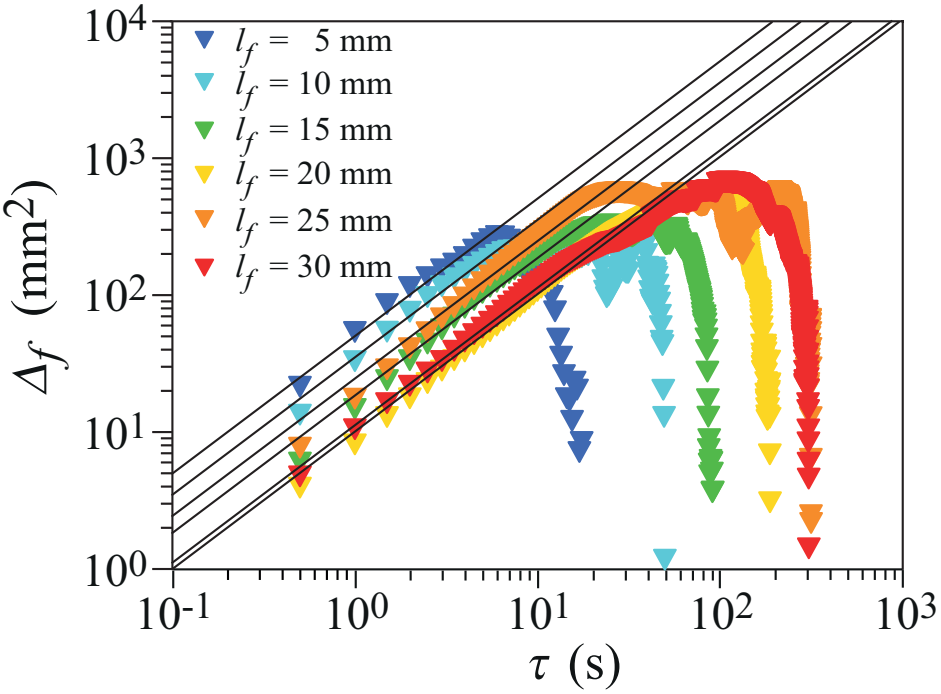

FIG. 8: MSD of a fiber, Δ_f, as a function of lag time, τ. Experimental conditions are: d_g =10 mm, d_f = 1.6 mm and ω = 0.5 rad.s^{-1}. Symbol colors indicate the length of the fiber l_f. Black lines correspond to the best fit of the data according to Eq. (8).

grain diameter to fiber length ratio, d_g/l_f. Each value of the fiber diffusion coefficient in this plot is averaged over measurements taken at different angular velocity of the paddle ω and fiber diameters d_f, since the normalized diffusion coefficient shows no significant dependence on these two parameters. Although the experimental data in Fig. 10(a) exhibit some dispersion, they align approximately along a linear trend, indicating that the diffusion coefficient of a single fiber within a granular flow can be expressed as:

$$K_f \simeq 0.1 \left(\frac{d_g}{l_f}\right) \frac{\dot{\gamma} d_g^2}{\sqrt{I}}. \tag{9}$$

This relationship is confirmed in Fig. 10(b), where the normalized diffusion coefficient is plotted against the ratio l_f/d_g in logarithmic scales, and a line with slope –1 provides a reasonable fit of the data. In Figs. 10(a) and (b), the diffusion coefficient for a grain in the granular flow, given by $K_g \simeq 0.03\,\dot{\gamma}\,{d_g}^2/\sqrt{I}$, is indicated by horizontal dashed lines. The measured diffusion coefficients for fibers are observed to be higher than the reference value for individual grains, indicating that fibers diffuse more rapidly within the granular flow. This enhanced diffusion may result from fibers' ability to align with the flow direction and their typically smaller diameters compared to the grains, allowing them to navigate through the pores between grains. Compared to grain diffusion, fiber diffusion introduces a single additional parameter: the length ratio l_f/d_g. This ratio also governs the sedimentation velocity of the fibers and appears to be the primary factor controlling fiber dynamics in granular flows. Nevertheless, further investigations are necessary to determine whether these findings hold across a broader range of conditions, such as when fibers have larger lengths or diameters.

IV. CONCLUSIONS AND PERSPECTIVES

In this study, we developed an experimental setup in which an index-matched granular medium is sheared by a paddle rotating about a vertical axis, enabling the investigation of the dynamics of a single fiber immersed within the granular flow. Our focus was on the quasistatic flow regime characterized by a large Stokes number, where the interstitial fluid plays a negligible role. We systematically explored the effects of key parameters—including imposed shear rate, grain size, and fiber dimensions (length and diameter)—on both grain and fiber dynamics.

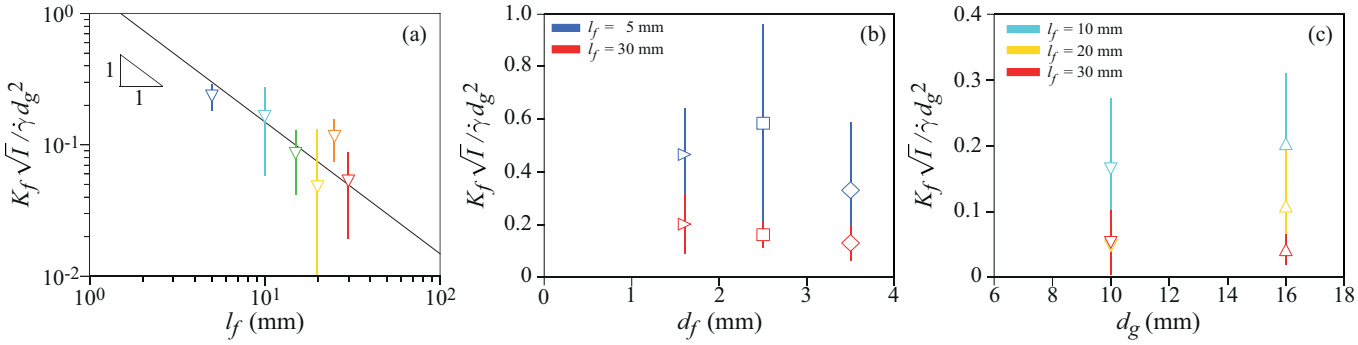

FIG. 9: Impact of fiber properties and grain size on fiber diffusion coefficient. Normalized diffusion coefficient $K_f\sqrt{I}/\dot{\gamma}{d_g}^2$ as a function of: (a) fiber length l_f, for fixed d_f = 1.6 mm, d_g =10 mm and ω = 0.5 rad.s^{-1}, (b) fiber diameter d_f, for two different values of l_f, with d_g =10 mm and ω = 1.2 rad.s^{-1} and (c) grain diameter d_g, for various values of l_f, with d_f = 1.6 mm and ω = 0.5 rad.s^{-1}. In panel (a), the solid line represents the best fit of the data with the relation: $K_f\sqrt{I}/\dot{\gamma}{d_g}^2 \propto l_f^{-1}$. The symbol color code corresponds to the fiber lengths, consistent with Fig. 7.

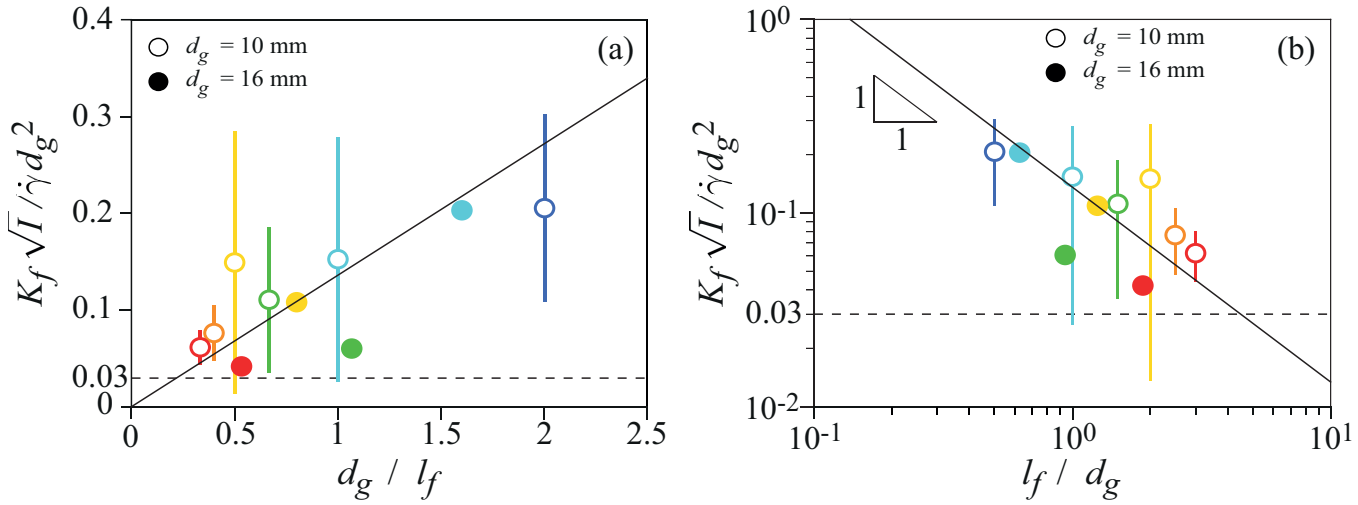

FIG. 10: Normalized diffusion coefficient $K_f\sqrt{I}/\dot{\gamma}{d_g}^2$ as a function of (a) d_g/l_f in lin-lin plot and (b) l_f/d_g in log-log plot. Solid line represents the equation of the form $K_f\sqrt{I}/\dot{\gamma}{d_g}^2 = Bd_g/l_f$ with $B = 0.1 \pm 0.01$. For a given value of d_g/l_f, the measurements were averaged over Ω and d_f. Symbol colors correspond to the fiber lengths l_f using the same color code as in Fig. 9. The horizontal dashed lines indicate the value of the grain diffusion coefficient, as given by Eq. (5).

Consistent with prior studies, we confirmed that individual grains exhibit diffusive motion along the vertical axis, with diffusion coefficients dependent on both grain diameter and shear rate. For the fiber, we observed a tendency to settle downward at a constant average velocity, which decreases exponentially with the fiber length to grain diameter ratio. After subtracting this mean settling velocity, the fiber's residual vertical motion was found to be diffusive, with its diffusion coefficient decreasing linearly as the fiber length to grain diameter ratio increases. Based on these observations, we proposed an empirical expression for the fiber diffusion coefficient within the granular medium.

These results offer a predictive framework for understanding fiber–granular mixing processes, relevant for manufacturing fiber-reinforced composites such as concrete, as well as natural materials like adobe and mortar. While this work focused on the dynamics of the fiber's center of mass, further studies are required to characterize fiber orientation, deformation, and the effects of additional parameters, including inter-particle friction, fiber bending stiffness, and the viscosity of the interstitial fluid.

ACKNOWLEDGEMENTS

The authors thank J. Amarni, A. Aubertin, L. Auffray, C. Manquest and R. Pidoux for their technical support. This work has benefited from fruitful discussions with Patrick Richard and Antonio Pol. This work has been supported by the project FiLiGran ANR 22-CE30-0012.

There are no conflicts to declare.

DATA AVAILABILITY

The data that support the findings of this article are openly available [37].

[1] J. M. Ottino and D. V. Khakhar, Mixing and segregation of granular materials, Annual review of fluid mechanics **32**, 55 (2000).
[2] A. M. Fry, P. B. Umbanhowar, J. M. Ottino, and R. M. Lueptow, Diffusion, mixing, and segregation in confined granular flows, AIChe Journal **65** (2019).
[3] R. Artoni, M. Larcher, J. T. Jenkins, and P. Richard, Self-diffusion scalings in dense granular flows, Soft Matter **17**, 2596 (2021).
[4] B. Utter and R. P. Behringer, Self-diffusion in dense granular shear flows, Physical review E **69**, 031308 (2004).
[5] P. Rognon and M. Macaulay, Shear-induced diffusion in dense granular fluids, Soft Matter **17**, 5271 (2021).
[6] R. Cai, H. Xiao, and J. Z. anf Yongzhi Zhao, Diffusion of size bidisperse spheres in dense granular shear flow, Physical Review E **99**, 032902 (2019).
[7] S. Athani, B. Metzger, R. Mari, Y. Forterre, and P. Rognon, Unifying suspension and granular shear-induced self-diffusion, J. Fluid Mech. **998** (2024).
[8] Y. Fan, P. B. Umbanhowar, J. M. Ottimo, and R. M. Lueptow, Shear-rate-independent diffusion in granular flows, Physical Review Letters **115**, 08801 (2015).
[9] C. S. Campbell, Self-diffusion in granular shear flows, J. Fluid Mech **348**, 85 (1997).
[10] V. Breedveld, D. van den Ende, M. Bosscher, R. J. J. Jongschaap, and J. Mellema, Measurement of the full shear-induced self-diffusion tensor of noncolloidal suspensions, Journal of Chemical Physics **116** (2002).
[11] S. Kumar, S. Khatoon, J. Yogi, S. K. Verma, and A. Anand, Experimental investigation of segregation in a rotating drum with non-spherical particles, Powder Technologies **411**, 117918 (2022).
[12] S. Kumar, S. Khatoon, P. Dubey, J. Yogi, and A. Anand, Shape-dependent radial segregation in rotating drum: Insight from dem simulations, Powder Technology **432**, 119134 (2024).
[13] D. Hernandez-Delfin, T. Weinhart, and R. C. Hidalgo, Self-diffusion of spherocylindrical particles flowing under non-uniform shear rate, Soft Matter **18**, 3335 (2022).
[14] Y. Liu, B. Chakrabarti, D. Saintillan, A. Lindner, and O. du Roure, Morphological transitions of elastic filaments in shear flow, PNAS **115**, 9438 (2018).
[15] M. Harasim, B. Wunderlich, O. Peleg, M. Kroger, and A. R. Bausch, Direct observation of the dynamics of semiflexible polymers in shear flows, Physical Review Letters **110**, 108302 (2013).
[16] J. K. N. Nan Xue and H. A. Stone, Shear-induced migration of confined flexible fibers, Soft Matter **18**, 514 (2022).
[17] U. Makanga, M. Sepahi, C. Duprat, and B. Delmotte, Obstacle-induced lateral dispersion and nontrivial trapping of flexible fibers settling in a viscous fluid, Phys. Rev. Fluids **8**, 044303 (2023).
[18] A. M. S lowicka, N. Xue, P. Sznajder, J. K. Nunes, H. A. Stone, and M. L. Ekiel-Jeżewska, Buckling of elastic fibers in a shear flow, New J. Phys. **24**, 013013 (2022).
[19] J. LaGrone, R. Cortez, W. Yan, and L. Fauci, Complex dynamics of long, flexible fibers in shear, Journal of Non-Newtonian Fluid Mechanics **269**, 73 (2019).
[20] L. Thian, G. Ahmadi, and J. Tu, Brownian diffusion of fibers, Aerosol science and technology **50**, 474 (2016).
[21] C. Tang, B. Shi, W. Gao, F. Chen, and Y. Cai, Strength and mechanical behavior of short polypropylene fiber reinforced and cement stabilized clayey soil, Geotextiles and Geomembranes **25**, 194 (2007).
[22] M. Anas, M. Khan, H. Bilal, S. Jadoon, and M. N. Khan, Fiber reinforced concrete: a review, Engineering Proceedings **22**, 3 (2022).
[23] `http://www.billeshydrogel.fr`.
[24] J. Barés, N. Brodu, H. Zheng, and J. A. Dijksman, Transparent experiments: releasing data from mechanical tests on three dimensional hydrogel sphere packings, Granular Matter **22**, 1 (2020).
[25] R. Tao, M. Wilson, and E. R. Weeks, Soft particle clogging in two-dimensional hoppers, Physical Review E **104**, 044909 (2021).
[26] J. Schindelin, I. Arganda-Carreras, V. K. Erwin Frise, M. Longair, T. Pietzsch, S. Preibisch, C. Rueden, S. Saalfeld, B. Schmid, J.-Y. Tinevez, D. J. White, V. Hartenstein, K. Eliceiri, P. Tomancak, and A. Cardona, Fiji – an open source plataform for biological image analysis, Nat Methods **9** (2019).
[27] D. B. Allan, T. Caswell, N. C. Keim, C. M. Van der Wel, and R. W. Verweij, Trackpy: v0.6.4, Zenodo (2024), `https://doi.org/10.5281/zenodo.16089574`.
[28] F. Boyer, É. Guazzelli, and O. Pouliquen, Unifying suspension and granular rheology, Physical review letters **107**, 188301 (2011).
[29] F. Tapia, C.-W. Hong, P. Aussillous, and É. Guazzelli, Rheology of suspensions of non-brownian soft spheres across the jamming and viscous-to-inertial transitions, Physical Review Letters **133**, 088201 (2024).
[30] F. da Cruz, S. Emam, M. Prochnow, J.-N. Roux, and F. m. c. Chevoir, Rheophysics of dense granular materials: Discrete simulation of plane shear flows, Phys. Rev. E **72**, 021309 (2005).
[31] A. Seguin, Y. Bertho, F. Martinez, J. Crassous, and P. Gondret, Experimental velocity fields and forces for a cylinder penetrating into a granular medium, Physical Review E **87**, 012201 (2013).
[32] M. Macaulay and P. Rognon, Shear-induced diffusion in cohesive granular flows: effect of enduring clusters, Journal of Fluid Mechanics **858**, R2 (2019).
[33] R. S. J. Bancroft and C. G. Johnson, Drag, diffusion and segregation in inertial granular flows, J. Fluid Mech. **924** (2021).
[34] N. Khola and C. Wassgren, Correlations for shear-induced percolation segregation in granular shear flows, Powder Technology **288**, 441 (2016).
[35] S. Gao, J. M. Ottino, P. B. Umbanhowar, and R. M. Lueptow, Percolation of a fine particle in static granular beds, Physical Review E **107**, 014903 (2023).
[36] S. Gao, J. M. Ottino, R. M. Lueptow, and P. B. Umbanhowar, Vertical velocity of a small sphere in a sheared granular bed, Physiscal Review Research **6**, L022015 (2024).

[37] K. N. C. Encarnación, Experimental data for diffusive motion of a semi-rigid fiber immersed in a granular flow [data set], Zenodo (2025), https://doi.org/10.5281/zenodo.15910124.